

Electronic complexity of active site models for FeNC catalysts: a systematic study of truncation effects in molecular and periodic models

Charlotte Gallenkamp,^a Young-Joon Song,^{b†} Niklas von Rhein^{a†}, Genís Lleopart Motis^c, Roser Valenti^b and Vera Krewald^{a*}

^a Technische Universität Darmstadt, Theoretische Chemie, Peter-Grünberg-Str. 4, 64237 Darmstadt, Germany;

^b Goethe-Universität Frankfurt, Institut für Theoretische Physik, Max-von-Laue-Str. 1, 60438 Frankfurt am Main, Germany;

^c Universitat de Barcelona, Departament de Ciència de Materials i Química Física and Institut de Química Teòrica i Computacional (IQTC), Martí i Franqués 1-11, 08028 Barcelona, Spain

†These authors contributed equally to this work.

* E-mail: vera.krewald@tu-darmstadt.de

While single-atom catalysts have been widely studied experimentally and computationally due to their high potential for small molecule activation reactions, the structures and electronic details of their active sites remain elusive. Much progress has been made with nuclei-specific spectroscopy methods, such as Mössbauer spectroscopy to probe FeNC catalysts for the oxygen reduction reaction. These studies are often complemented by computational studies on active site models. We here report on the optimal model size for computational studies of FeNC catalysts with molecular and periodic approaches using two prominent FeNC active site models, $\text{FeN}_4\text{C}_{10}$ (pyridinic nitrogen coordination) and $\text{FeN}_4\text{C}_{12}$ (pyrrolic nitrogen coordination). We furthermore unveil the electronic complexity of these models to include not only the expected low spin, intermediate spin and high spin configurations, but in addition intrasystem redox events and unpaired electrons in the graphene-like environment that ferromagnetically or antiferromagnetically couple with the unpaired electrons located on iron. A key conclusion is that square-planar structures fail to explain the experimentally observed high spin species. Instead, axial displacements of iron or binding of axial ligands are needed to stabilise the high spin configuration, which has implications for the interpretation of experimental data and thus the mechanism of the oxygen reduction reaction.

1 Introduction

With growing concerns about global warming being a major challenge of our time, alternatives to fossil fuel are sought across many branches of science. One approach is the improvement of fuel cell technology.^{1–4} In hydrogen fuel cells, the high demand for platinum catalysts for the two electrochemical half-reactions limits both sustainability and roll-out on a large scale.^{1,3,5,6} Especially for the kinetically hindered oxygen reduction reaction (ORR), where four electrons are transferred, the platinum load is high.^{5–8} In the search for alternative catalysts, single-atom metal-N-C catalysts^{9,10} and among them especially FeNC catalysts,^{5–7,11–15} have been found promising and hence became a highly active field of research.

Due to a pyrolysis step in their preparation, FeNC catalysts are amorphous materials and thus knowledge about the structural composition of their active site(s) is limited^{5,6,11–14,16}.

Nuclei-specific spectroscopy methods, such as X-ray absorption spectroscopy^{9,12,14,17,18} or Mössbauer spectroscopy^{5,6,11,19–23} are thus required for structural elucidation. Because of the detailed information on iron oxidation and spin states offered by Mössbauer spectroscopy, it has been used especially extensively to study FeNC catalysts. A Mössbauer doublet signal is characterized by the isomer shift and the quadrupole splitting. The isomer shift depends linearly on the s-electron density at the nucleus, while the quadrupole splitting is defined by the electric field gradient, making it highly sensitive to the symmetry of the electron distribution around the nucleus.^{24–27} Both Mössbauer parameters show a temperature dependence, making low temperature experiments on FeNC catalysts highly relevant for comparisons with computational data that are formally carried out at 0 K.^{6,28}

The currently dominant perspective on active sites in FeNC catalysts is that iron atoms are surrounded by a fourfold nitrogen coordination sphere that are embedded in a carbon matrix, which is assumed to be graphene-like^{5,6,11,12,14,20–22,29}. However, questions regarding the type of N-donor, the presence and nature of axial ligands, the oxidation state (Fe(II) or Fe(III)) and the spin state of iron are still being debated.^{5,6,11,20–22,29,30} Recent *in situ*^{5,6,31} – measuring the catalyst in an electrochemical cell with an applied potential – and *operando*^{6,31,32} – experiments under applied potential and oxygen saturation – Mössbauer studies on FeNC catalysts shed light on the different species appearing during the ORR oxidation cycle. The *in situ* conditions showed spectroscopic signatures of iron high spin states which have been attributed to the active site.^{5,6,31,32}

The interpretation of experimental spectroscopy data is often supported by quantum chemical studies of model systems.^{3,5,6,11,20,21,29,30,33} Both molecular^{5,6,11,20,29,30,34–39} and periodic^{33,34,36,40–45} calculations can be used for structural elucidation of FeNC catalysts, where both approaches have strengths and weaknesses.³⁶ Molecular models are structurally flexible and allow for direct comparisons with experimentally available porphyrin and phthalocyanine complexes for which Mössbauer parameters and other spectroscopic properties have been studied extensively.^{46–51} Due to the associated computational cost, the π system that can be considered in molecular models is limited. It is therefore unclear whether the graphene-like structure assumed in FeNC catalysts is represented appropriately.^{11,12,14} Periodic models incorporated with

atomic and/or plane-wave basis sets are suitable for large crystalline systems and detailed analyses of electronic and magnetic structures. Here, too, the computational cost associated with a larger system size limits the extent of the graphene-like layer that the active site is embedded in, which may lead to artificially interactions between iron atoms in adjacent unit cells. For both model types, it is thus important to identify a sufficient model size, which has not been systematically evaluated to date.

The expected size of the structural models of several dozen atoms limits the electronic structure methods that can be applied. Wavefunction methods cannot be used due to their high computational cost even though iron is notorious for its often multireference electronic structures due to partially occupied d-orbitals and many accessible electronic states.^{52–57} Instead, FeNC catalyst models are usually studied with density functional theory.^{11,37,58} Nevertheless, the electronic complexity of iron warrants a comprehensive view of all probable electronic structures and spin states in FeNC models.^{43,45,57}

In this work, we investigate two typical FeNC active site models with density functional theory: the pyridinic-type $\text{FeN}_4\text{C}_{10}$ (model **A**) and the pyrrolic-type $\text{FeN}_4\text{C}_{12}$ (model **B**), see Figure 1. We employ both molecular and periodic techniques to systematically study the influence of system size on the convergence behavior of spin state energetics and Mössbauer parameters. The electronic structures resulting from periodic and molecular descriptions are compared in detail. Importantly, we find that several electronic structures are energetically accessible, some of which feature unpaired electrons in the carbon matrix. This degree of electronic complexity has not been established for FeNC catalysts so far. Furthermore, we demonstrate that iron high spin states are not energetically accessible in square-planar FeNC models, and show that axial distortions of the iron atom from the graphene plane or the binding of axial ligands are needed to explain the experimental observations.

2 Computational Details

Density functional theory⁵⁹ (DFT) calculations for molecular models were performed using the ORCA program suite with the unrestricted Kohn-Sham formalism (UKS).⁶⁰ The size variations of a 2+ charged model **A** and a neutral model **B** were investigated using ORCA 4.2^{61,62}. Calculations on models without axial ligand containing 36 (**A**) and 52 (**B**) carbon atoms (system size 4) were rerun for a thorough spin state investigation with ORCA 5.0.^{61,62} ORCA 5.0 was also used for the size variation of models with axial ligands.

All calculations used “tight” SCF convergence criteria in ORCA nomenclature, the SMD⁶³ solvent model with water and the split-RI-J approximation (for generalized gradient approximation (GGA) and meta-GGA functionals) or the RIJCOSX-approximation⁶⁴ (hybrid functionals) with the auxiliary basis set def2/J⁶⁵. ORCA 5.0 calculations used the predefined integration grid “DefGrid2”. ORCA 4.2 calculations used an angular grid of size 6, with an increased grid size of 7 and an intacc setting of 7.0 for the iron atom in single point and Mössbauer calculations.

All geometries were optimized using the meta-GGA density functional TPSS⁶⁶ with a def2-SVP basis set C and H, a def2-TZVP⁶⁷ basis set on all other atoms, a Grimme-D3-dispersion correction⁶⁸ with Becke-Johnson damping⁶⁹ and “tight” con-

vergence criteria in OCRA nomenclature. Frequency calculations were used to make sure to find true energetic minima. Energies were calculated with the OPBE GGA functional^{70,71} (ORCA 5.0) or the OLYP GGA functional^{71,72} (ORCA 4.2), the CP(PPP)⁷³ basis on iron, def2-TZVP basis sets on all other atoms and no dispersion correction. Mössbauer parameters were calculated using the B3LYP hybrid functional,^{72,74} a Grimme-D3 dispersion correction with Becke-Johnson damping and the same basis sets as the energy calculations. Calibration of the Mössbauer parameter prediction performed by Gallenkamp *et al.*¹¹ for ORCA 4.2 and an analogous in-house calibration study for ORCA 5.0 resulted in trust regions of $\pm 0.13 \text{ mm s}^{-1}$ for the isomer shift and $\pm 0.36 \text{ mm s}^{-1}$ (ORCA 4.2) and $\pm 0.22 \text{ mm s}^{-1}$ (ORCA 5.0) for the quadrupole splitting. UCSF ChimeraX⁷⁵ was used to create molecular graphics.

For periodic models, the projector augmented wave (PAW) method⁷⁶ implemented in Vienna Ab initio Simulation Package (VASP)⁷⁷ was employed. To treat the exchange-correlation functional, we utilized the PBE⁷⁰ GGA functional and GGA with on-site Coulomb repulsion U (GGA+ U)⁷⁸ to account for localized 3d orbitals accurately. The first Brillouin zone was sampled using a Gamma-centered $4 \times 4 \times 1$ k -mesh for structure relaxation, while denser k -mesh values of $21 \times 21 \times 1$ (for the 4×4 unit cell), $15 \times 15 \times 1$ (for 6×6), and $9 \times 9 \times 1$ (for 8×8) were chosen for single-point calculations. The plane-wave basis set size was determined by the energy cutoff of 400 eV (500 eV) for relaxation (single-point calculations). All atomic positions were fully relaxed until the net force became smaller than 0.01 eV/Å. To prevent interactions between layers along the crystallographic c -axis, a 20 Å vacuum layer was introduced in all structures. However, for cases with the axial 2-MeHIm ligand, the vacuum thickness was increased to 30 Å.

Additionally, we included the use of hybrid functionals for periodic models, which have been widely used in computational chemistry and materials science for studying diverse systems ranging from small molecules and molecular complexes to bulk materials and surfaces⁷⁹. For hybrid functionals, we employed the highly parallelized Fritz Haber Institute ab initio materials simulations (FHI-aims) software⁸⁰, which employs all-electron numerical atom-centered (NAO) basis functions for its electronic structure calculations for ensuring highly accurate results. In all our calculations involving FHI-aims, we employed Tier 1 light basis set, which has been shown to provide results of similar or higher quality to those obtained using a triple-zeta plus polarization Gaussian-type orbitals (GTOs) basis set⁸¹. While the heavy computational cost of hybrid functionals has been studied and justified moving to less demanding DFT approaches⁸², in the last recent years it has been shown how incorporation of hybrid functionals in extremely large systems are feasible employing FHI-aims⁸³.

3 Results and discussion

3.1 Fourfold coordinated models $\text{FeN}_4\text{C}_{10}$ and $\text{FeN}_4\text{C}_{12}$

3.1.1 Systematic investigation of electronic structures

The electronic structure of iron in (pseudo-)molecular environments is notoriously complex due to different spin states that are easily energetically accessible within the same oxidation state.^{52–57,73} Moreover, different oxidation states can be attained readily, including by intramolecular redox events with so-called redox non-innocent ligands.^{84–86} Even within the

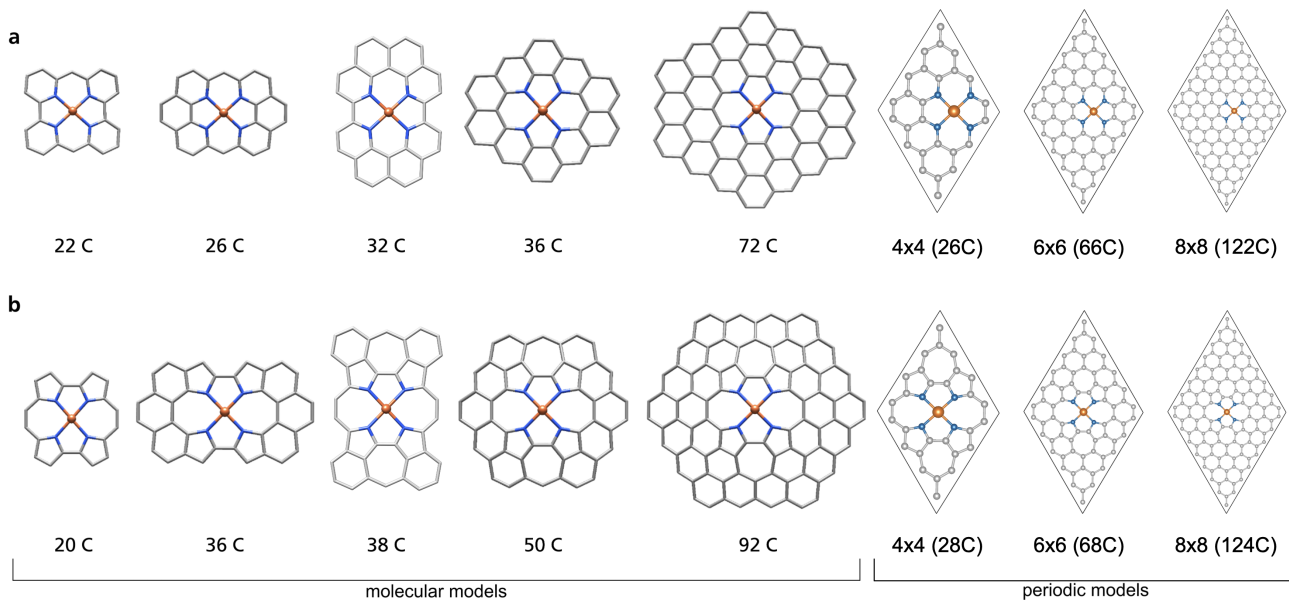


Figure 1 Structures of the size variation for fourfold coordinated models **A** $\text{FeN}_4\text{C}_{10}$ (pyridinic) and **B** $\text{FeN}_4\text{C}_{12}$ (pyrrolic). The number of carbon atoms is given for molecular models and the size of the supercell is given for periodic models.

same oxidation and spin state, details of the electronic structure can differ due to the orbital occupation pattern, which is dictated by the ligand field splitting and thus ultimately the local geometry around the iron ion. For an FeN_4 -system with an iron(II) ion, six electrons are expected to occupy the d-orbitals. In addition, the conjugated π -system of the equatorial ligand can play a role by hosting unpaired electrons, either by intramolecular redox events (formally oxidising the iron ion to Fe(III)) or by being in a triplet configuration that couples ferromagnetically or antiferromagnetically with the unpaired electrons of the iron ion.

We investigated two types of model, the pyridinic-type model **A** ($\text{FeN}_4\text{C}_{10}$) and the pyrrolic-type model **B** ($\text{FeN}_4\text{C}_{12}$), see Figure 1 and SI. In model **A**, the incorporation of nitrogen in pyridinic, six-membered rings results in the preservation of a fully planar, graphene-like structure for all system sizes. The iron nucleus is therefore coordinated in a square-planar environment; only in model size 2, the iron is moved substantially out of plane (0.6 Å in the HS1 state), leading to a slightly bent structure of the equatorial ligand. In model **B**, the pyrrolic, five-membered rings require the incorporation of defects within the graphene plane. We introduced seven-membered rings within the first shell of carbon atoms which results in a possible break of planarity.⁸⁷ The planarity changes with the system size: while system sizes 1 to 3 are fully planar, system sizes 4 and 5 are convex models with the iron being moved slightly (approx 0.1 Å for model size 5, HS1) out of plane compared to a square-planar coordination environment. The model geometries and structural parameters are given in the SI.

We identified eight relevant electronic configurations, the possible orbital occupation patterns of which are sketched in Figure 2. The ground state configuration is an intermediate spin (IS) Fe(II) where the d_{xy} and d_{yz} orbitals are doubly occupied, the d_{xz} and d_{z^2} are singly occupied, and the $d_{x^2-y^2}$ orbital is unoccupied, labeled IS3 in Figure 2. This is in agreement with expectations for fourfold coordinated $\text{Fe}(\text{II})\text{N}_4$ systems.⁴⁶

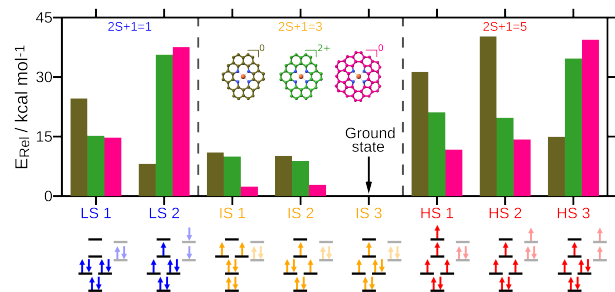


Figure 2 Relative energies of several possible spin states for model A^0 (olive green), A^{2+} (light green) and B (pink). The orbital occupation patterns of the spin states are sketched below, where low spin states are shown in blue, intermediate spin states in yellow and high spin states in red. Note that for LS2 and HS3 of model A^{2+} and B as well as HS1 and HS2 of model A^0 , negative HOMO-LUMO gaps are found. For HS2 of A^0 , the optimized geometry of HS1 had to be used.

As d_{xz} and d_{yz} are near-degenerate in the systems investigated here, additional configurations with low-lying energies were found. In IS1, the unpaired electrons are located in d_{xz} and d_{yz} ; in IS2, they are in d_{yz} and d_{z^2} . IS2 and IS3 differ only slightly in the occupations of the strongly hybridized orbitals and may be difficult to discern in terms of the molecular orbital composition. They can, however, be distinguished using the quadrupole splitting (see Figure 3): IS2 has a lower quadrupole splitting than IS3 in all three models. The near-degeneracy of d_{xz} and d_{xy} and the possibly energetically close lying states IS1 and IS2 to IS3 can lead to a multireference character in FeN_4 systems, especially if the local ligand field of the iron ion is square-planar.

For the total multiplicities of $2S+1 = 1$ (LS) and 5 (HS), one electronic configuration is found if the ligand remains closed-shell. In LS1, all electrons are paired and found in the three lowest-lying d-orbitals. In HS1, all five d-orbitals are occupied, the lowest-lying one being doubly occupied. With two unpaired electrons in the π -system, additional configurations

arise: in LS2 they are antiferromagnetically coupled and in HS3 they are ferromagnetically coupled to an intermediate spin Fe(II) of type IS3. An additional HS configuration, HS2, is characterized as an intramolecular redox event with one electron transferred from the iron center to the delocalized π -system, rendering the iron ion in an Fe(III) intermediate spin configuration.

To study the influence of the graphene-like environment on the preferred spin state and Mössbauer parameters, we tried to identify all of the electronic configurations described above in an initial screening step using the model sizes shown in Figure 1. As discussed below, the properties of the models converge at size 4 (36C/50C for models A/B respectively), for which these electronic structures and their Mössbauer parameters are discussed exemplarily.

In the planar model A^0 , the two variants of the ground state IS3 configuration with triplet configurations on the ligand, LS2 and HS3, are found within 15 kcal/mol. The two alternative intermediate spin configurations IS1 and IS2 lie within 11 kcal/mol. The remaining electronic structure types, LS1, HS1 and HS2, are destabilized by more than 24 kcal/mol. Notably, the electronic structures of HS1 and HS2 have negative HOMO-LUMO gaps, i.e. appear to be excited states with respect to IS3.

In the charged planar system A^{2+} , the IS1 and IS2 configurations are found at 9-10 kcal mol⁻¹ compared to the IS3 ground state. In contrast to the neutral model, LS2 and HS3 are highly destabilized with negative HOMO-LUMO gaps. The other electronic structure types are found at least 15 kcal/mol above the IS3 ground state. Differences between the charged model A^{2+} and the neutral model A are expected to arise from fewer π orbitals being occupied in the equatorial ligand, so that ring-open-shell electronic structures like LS2 or HS3 will experience different stabilizations.

For the non-planar system **B**, all three types of IS are found within 3 kcal/mol of each other, making multireference character plausible. LS1, HS1 and HS2 have relative energies of about 10-15 kcal/mol while LS2 and HS3 lie considerably higher in energy. We note that LS2 and HS3 could only be obtained by enforcing orbital occupations with a negative HOMO-LUMO-gap, i.e. locally excited states, leading to the assumption that a concave structure destabilizes such ring open shell systems. This can in part be explained by “classical” high- and low spin states LS1 and HS1 being stabilized by non-planar structures.⁴⁶ Furthermore, the bent structure might lead to lower overlap of the iron d-orbitals and the ring orbitals, making a distribution of spin density on the ring less favourable.

Turning to the Mössbauer parameters of energetically relevant configurations, see Figure 3, it is clear that IS3, HS3 and LS2 behave similarly. This is not surprising given their similar electronic structures at the iron atom; the unpaired electrons on the ring have a limited influence on the Mössbauer parameters. The isomer shifts of the three IS configurations lie within the uncertainty range of the calibration study, which is consistent with their nearly identical structural parameters. Their quadrupole splitting values differ more significantly, which is expected due to the different orbital occupations and hence different symmetries of the electric field gradient. For A^{2+} /**B**, the electronically distinct configurations LS1/LS1 and HS1, respectively, fall close to the IS3 reference value. For **B**, the HS2 configuration arising from the intramolecular redox event has a clearly distinguishable Mössbauer signature.

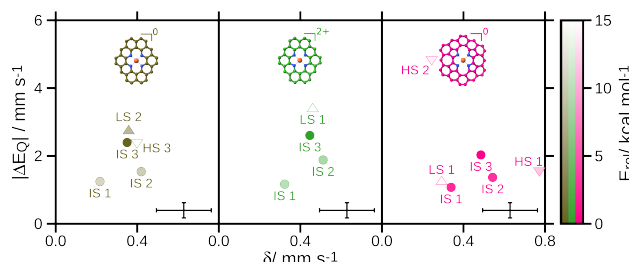


Figure 3 Mössbauer parameters of selected electronic structures for model A^0 (olive green), A^{2+} (light green) and **B** (pink). The intensity of the color is scaled with the relative electronic energy of the structure. The data points are labeled with the respective spin state (upward triangles: LS, circles: IS, downward triangles: HS). The computational uncertainty of the Mössbauer parameters is shown in the lower right corner of each panel. Only states with relative energies below 16 kcal mol⁻¹ are shown, see SI for full data.

3.1.2 Size variation of molecular models

The fact that different electronic configurations with possibly considerably different Mössbauer parameters are accessible demonstrates that a thorough investigation of their importance in different sizes of graphene-like environment is warranted if a full picture of the Mössbauer behaviour of model complexes for FeNC catalysts is to be obtained.

The dependence of spin state energetics and Mössbauer parameters on the size of the molecular model is shown in Figure 4 for A^{2+} and **B**. Strikingly, no true high spin (HS 1) or low spin (LS 1) state appears within 10 kcal mol⁻¹ for any of the model sizes. This is an important observation since high spin Fe(II) is observed as a key signature in FeNC catalysts and has often been attributed to models of this type.^{5,6,22,31} Intermediate spin states, that are expected from a ligand field perspective, as well as ring-open-shell high spin (HS 3) and intramolecular redox high spin states (HS 2) are predicted to be low-lying, possibly even as a ground state configuration.

Within the same electronic configuration, the Mössbauer parameters converge rapidly with system size. Within the same state, the largest difference in Mössbauer parameters is seen between model sizes 2 and 3, which can be attributed to the different symmetries of these models that affect the quadrupole splitting in particular.

For A^{2+} , IS3 is always the electronic ground state, except for system size 2, where HS3 is found to be more stable. At system size 5, HS3 is energetically low lying, probably due to the ring open-shell character being stabilized by the extended π system. Since the Mössbauer parameters of HS 3 and IS 3 are indistinguishable within the uncertainty ranges of the isomer shift and quadrupole splitting, the two configurations could probably not be discerned experimentally. Therefore, for model A^{2+} , a convergence can be assumed for system size 4. For model **B**, the electronic ground state converges more slowly. One reason is the change in planarity of the graphene environment: while for system sizes 1 to 3, the graphene plane is planar, it is concave for system size 4 and 5. This means that for structural convergence, at least system size 4 is necessary. At system sizes 4 and 5, all three intermediate spin states are found within 5 kcal mol⁻¹.

Overall, convergence of the structural parameters, ground spin state and Mössbauer properties is reached at system size four (36 and 50 carbon atoms for model A^{2+} and **B**, respec-

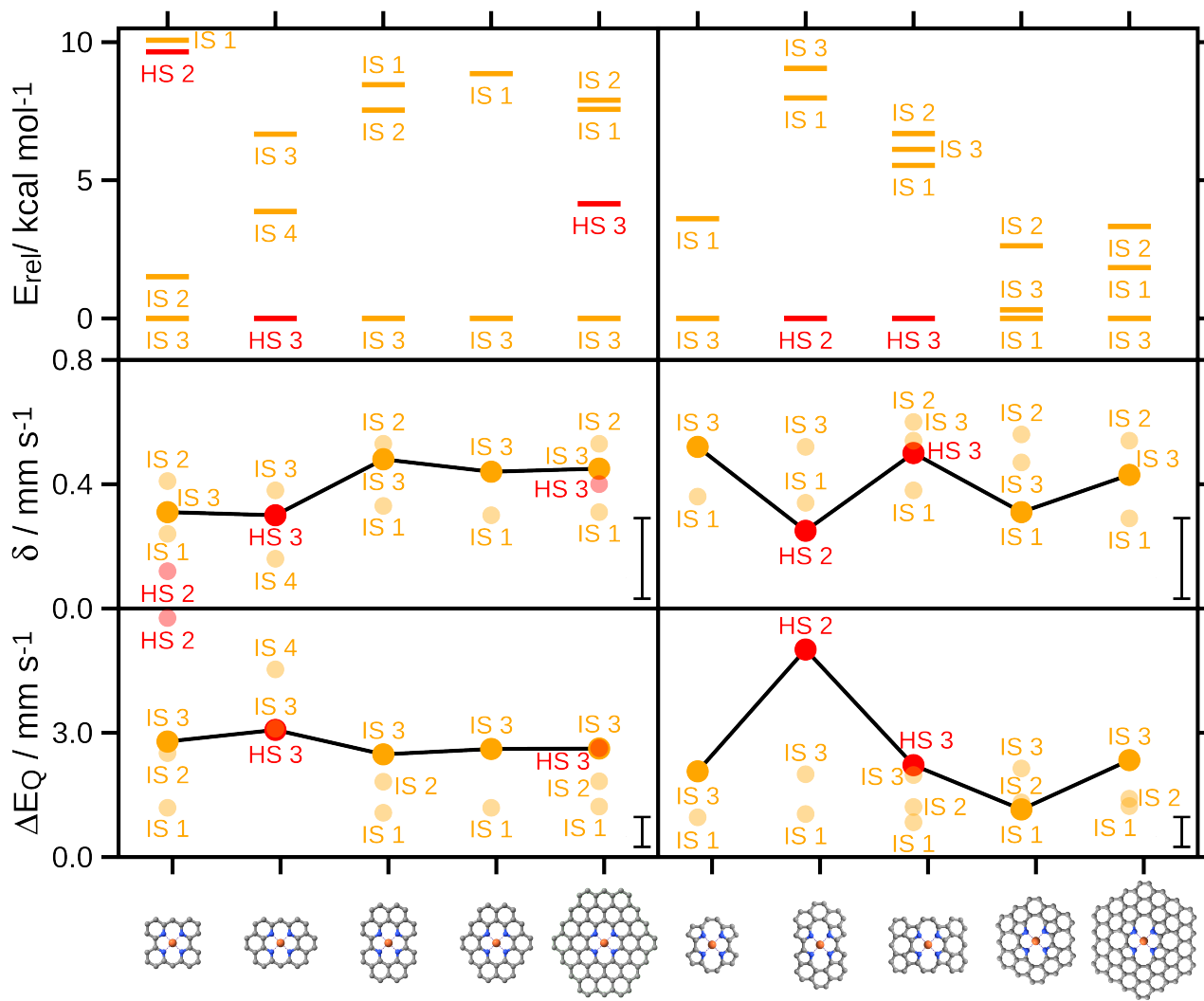


Figure 4 Evolution of spin state energetics (top) and Mössbauer parameters (middle, bottom) of a charged model A^{2+} (left panels) and a neutral model B (right panels). In the upper panels, all states with a relative energy $< 10 \text{ kcal mol}^{-1}$ are shown, labeled according to Figure 2. Intermediate spin states are shown in yellow and high spin states in red. The connected data points correspond to the electronic ground state; the unconnected, transparent data points to energetically low-lying configurations. Uncertainty ranges of the respective Mössbauer parameters are shown in the lower right corners.

tively). At this model size, two full carbon rings around the FeN_4 center are included. A further increase in the system size was found unlikely to produce results that would justify the significant increase in computational cost.

3.1.3 Analysis of the electronic and magnetic structures in periodic FeN_4C_x

To complement the analysis above based on molecular models, periodic models were constructed in three sizes ($n \times n$ with $n = 4, 6$, and 8), and then fully relaxed. We note that the periodic models have an overall neutral charge. As was shown with the molecular models, the relevant IS configurations of A and A^{2+} behave very similarly, especially those that are spectroscopically discernible.

When using periodic boundary conditions, one needs to examine the size of the unit cell to minimize the interaction between two adjacent iron atoms. In the 4×4 model, the distance between two iron atoms amounts to 9.73 \AA (10.11 \AA) in the

pyridinic (pyrrolic) structure. Inspection of the spin density near the unit cell boundary suggests that this distance is too short to avoid iron-iron interactions, especially in the pyrrolic case, see Fig. 5 (a) and (b). In the 6×6 model where the neighboring iron distance increases to 14.70 \AA (14.96 \AA), the spin density around the iron atom no longer extends to the unit cell boundary. As shown in Fig. 6, enlarging the unit cell significantly reduces the bandwidth of both d_{yz} and d_{xz} orbitals, as discussed further below. This trend continues for the 8×8 model, so that a unit cell of at least size 6×6 can eliminate potential iron-iron interactions in periodic models.

As a second technical aspect, we note that the standard GGA functional often fails to accurately describe the exact ground state for iron due to the spatial compactness of the d -orbitals. Including an on-site Coulomb repulsion term U in calculations is one way to properly handle $3d$ orbitals.⁸⁸ This was recently discussed by us in detail for FeNC models.³⁶ For selected cases below, we explore the use of GGA+ U and the incorporation of

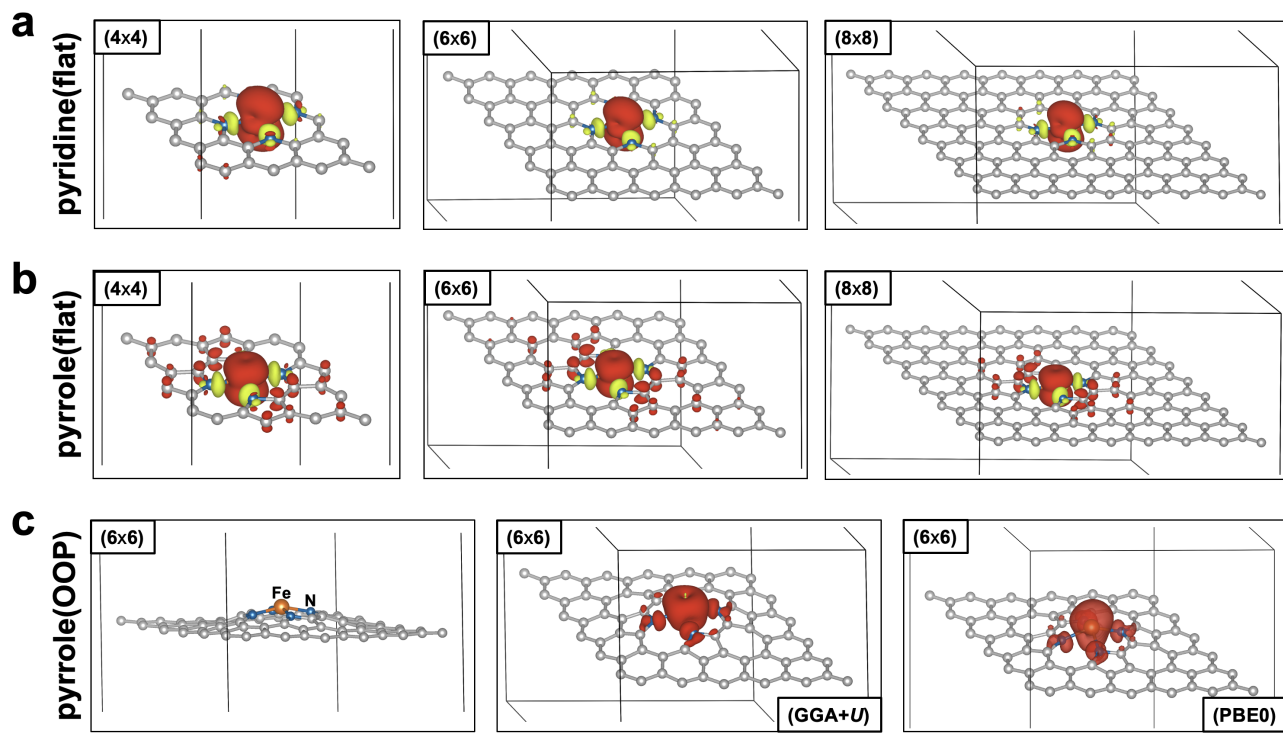


Figure 5 Spin density ($\rho_{\uparrow} - \rho_{\downarrow}$) of the $n \times n$ ($n = 4, 6$, and 8) (a) pyridinic and (b) pyrrolic flat structures within spin-polarized GGA. (c) The relaxed 6×6 pyrrole OOP structure (left) and the corresponding spin density obtained using GGA+ U (middle) and the PBE0 hybrid functional (right). The unit cell of each structure was cut to show the spin density near the iron site. The red color indicates positive density while negative density is in bright green. Isovalue is $0.01 \text{ e}/\text{\AA}^3$ for all.

exact Hartree–Fock exchange (HFE) in the PBE0 hybrid functional.

Starting with model size 6×6 within GGA, the total magnetic moments (M_{tot}) of the pyridinic and pyrrolic models are $1.97 \mu_B$ and $2.20 \mu_B$, corresponding to the $2S + 1 = 3$ intermediate spin configuration. These values result from different orbital occupations, see Figure 5 (a) and (b) for the spin densities. The pyridinic model A is found in an IS3 configuration. Consequently, the shape of the spin density is determined by a combination of both d_{xz} and d_{z^2} orbitals, see Figure 5. We note that the local axes used to describe cubic harmonics in the periodic models are rotated by 45° with respect to the crystallographic c -axis compared to those in the molecular models. As a result, the lowest occupied orbital in the periodic model is $d_{x^2-y^2}$, whereas it is d_{xy} in molecular models in the respective reference frame, but note that it is the same orbital. The pyrrolic model B is found in the IS1 configuration, resulting in a spin density shape that contains d_{xz} and d_{yz} contributions. These intermediate spin configurations remain unchanged when employing the GGA+ U or PBE0 hybrid functional, as shown in Figures S3 and S4 in the SI.

To gain insight into this difference in the orbital occupations, we analyzed the non-spin-polarized GGA results, excluding the effects of magnetism. Figure 6 presents the iron $3d$ orbital-resolved partial density of states for the 6×6 pyridinic (model A) and pyrrolic (model B) flat structures, along with their schematic energy centers of each $3d$ orbital. Contrary to the 4×4 structures as shown in Fig. S2, where both d_{yz} and d_{xz} orbitals are dispersive in both models, all orbitals in the enlarged 6×6 structures become localized, sitting near the Fermi energy except for d_{xy} . As mentioned above, this fact in-

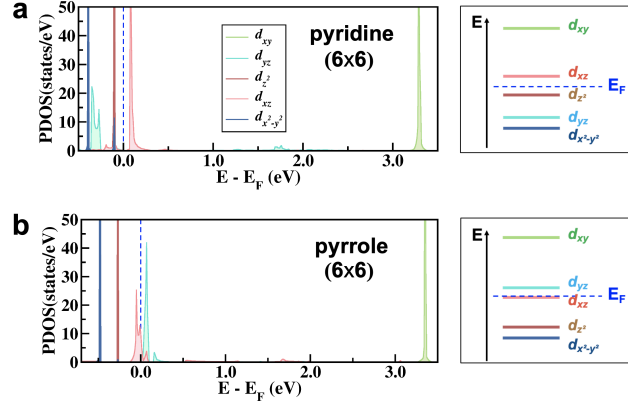


Figure 6 Partial densities of states projected on the iron $3d$ orbitals of the 6×6 (a) pyridinic and (b) pyrrolic flat structures within non-spin-polarized GGA. The Fermi level is set to zero. On the right side, the energy centers of each orbital are schematically depicted.

dicates that potential interactions between neighboring iron atoms are minimized. The d_{xy} orbital is strongly destabilized with a huge gap of about 3eV due to the $pd\sigma$ -antibonding interaction between Fe d_{xy} and N $p_{x/y}$ orbitals, and the $d_{x^2-y^2}$ orbital is always the most stabilized. Considering the rotation of the axis system with respect to the molecular models, this is in full agreement with the results presented in the previous section with the molecular model. For the pyridinic case, the energetic sequence, and hence the orbital occupation pattern, of the d_{yz} , d_{z^2} and d_{xz} orbitals is similar to the molecular models. In the pyrrolic model, a different energetic sequence is

found in the periodic model compared to the molecular model, specifically the d_{z^2} orbital being more stabilized. This leads to an IS1 ground state for the periodic model compared with an IS3 ground state in the molecular model. Since the iron and nitrogen distances differ by only 0.017 Å between the periodic models with pyridinic and pyrrolic nitrogen donors, we trace this difference to the enforced planarity of the periodic models. More specifically, nuances in the ligand field splitting of the iron 3d orbitals likely stem from the surrounding carbon environment given the high structural similarity of the immediate FeN_4 units. Therefore, the two distinct nitrogen environments appear to generate different ligand fields, leading to different orbital occupations of the iron 3d orbitals with an overall $2S+1 = 3$ intermediate spin configuration, see Figure 5.

To identify whether a bent geometry is feasible in the periodic models, we manually placed the iron atom 0.85 Å above the carbon layer of the relaxed pyridinic and pyrrolic structures, and then fully relaxed them using GGA+U. A bent geometry is found only for the pyrrolic cases, while the pyridinic case prefers to remain flat. In this ‘out-of-plane’ (OOP) phase of the pyridinic model, the iron atom is found 1.15 Å above the layer, accompanied by a 7.3% increase in Fe–N distances to 1.99 Å compared to the flat 6×6 pyrrolic structures, see Figure 5(c). Within GGA+U, the most stable spin state in the 6×6 OOP graphene environment is a $2S+1 = 5$ high spin configuration: the d_{z^2} orbital is now doubly occupied, whereas the other orbitals remain singly occupied. According to our non-spin-polarized GGA results, unlike the flat 6×6 pyrrolic structure where a sizable energy gap of approximately 3eV is calculated between the highest-lying orbital (d_{xy}) and the second highest-lying one (d_{yz}), this gap is significantly reduced to about 2 eV in the OOP phase, likely enabling a high-spin state. The vertical distance between the graphene layer and the iron atom is slightly reduced in the 4×4 case to 0.72 Å, whereas it increases to 1.46 Å in the 8×8 case. According to the GGA+U results, the OOP phase is energetically destabilised by 81 meV (≈ 1.87 kcal/mol) compared to the flat model. This difference is much larger (464 meV ≈ 10.7 kcal/mol) using GGA. Using the hybrid functional PBE0, a similar high spin configuration can be found with a different shape on the d-orbital of Fe atom (see Figure 5 (c)). A detailed observation when comparing the electronic structure of pure-GGA PBE functional and PBE0 hybrid functionals indicates how incorporation of HFE in combination with OOP distortion induces and stabilizes high-spin solutions on Fe center (analysis of the projected density of states for the flat and OOP pyrrolic models can be found in SI). We can surmise that even though the OOP phase is less stable and would not be thermodynamically viable compared to the flat phase, it may be stabilized by binding axial ligands or external constraints such as curving the graphene matrix in a carbon nanotube. Furthermore, our GGA+U results confirm a 2.3% decrease in work function in the 6×6 OOP compared to the flat structure, which could influence chemical reactivity between iron and adsorbates.

Both computational approaches -molecular and periodic models- thus predict an intermediate spin state for square-planar iron environments, despite differences in the specifics of the orbital occupation pattern in the pyrrolic case. An intermediate spin state is expected for square-planar coordination environments from ligand field theory considerations, and emphasizes that the computational treatment of the carbon environment does not influence the energetically preferred spin

state. We thus conclude that assignments of a high-spin species observed experimentally cannot be made to FeNC models without axial ligands or a significant curvature of the carbon environment.

3.2 Fivefold coordinated models $\text{FeN}_4\text{C}_{10/12}\text{-Cl}$ and $\text{FeN}_4\text{C}_{10/12}\text{-2-MeHIm}$

Typical signatures in *in situ* Mössbauer experiments on FeNC catalysts are indicative of Fe(II) high spin and Fe(III) sites.^{5,6,31,32} These signatures cannot be explained by our fourfold-coordinate iron(II) models, where high spin states are strongly destabilized. Therefore, we investigated models with an additional axial ligand. Fivefold coordinated complexes such as $[\text{Fe}(\text{TPP})(2\text{-MeHIm})]$ ⁴⁷ and $[\text{Fe}(\text{TPP})(\text{Cl})]$ ⁵⁰ have been discussed in the literature as model complexes for FeNC catalysts and as active catalysts themselves. While these specific axial ligands may not be present in FeNC catalysts obtained by pyrolysis, they are representative in terms of ligand field strength and type of interaction that can be reasonably expected in the real catalysts. As the reference systems in the literature are neutral,^{47,50} we also assumed an overall neutral charge for our model systems.

Adding an axial 2-MeHIm ligand to the pyridinic models maintains an intermediate spin state, see Figure 7. Consequently, the isomer shift is converged within the uncertainty range at all model sizes, and the quadrupole splitting is converged at model size 4, probably due to its symmetry dependence and the asymmetry of size 2 and 3. No true high spin state is energetically accessible at any model size. The experimentally observed iron(II) high spin signals can thus not be explained with this pyridinic model, as is supported by Ni, Gallenkamp *et al.*^{5,6} This can be explained with the structure of the A-2-MeHIm complex, where the iron is strictly in plane with the carbon environment, destabilizing high spin states⁴⁶. The axial ligand is thus not sufficient to significantly alter the ligand field and stabilize the highest lying d-orbital.

For model B, the ground state varies more in models of different size. While an intermediate spin state can always be found within a few kcal/mol of the ground state, the preferred electronic structure can also be described as an internal redox event, a ring-open-shell electronic structure, or a high spin configuration. The small energy differences between IS and HS state show that high spin states are energetically accessible in this type of model. We note that they may mix with intermediate spin states, as multireference character cannot be excluded. Overall, model B-2-MeHIm is more likely to explain the experimentally observed Fe(II) high spin signals, as was also concluded by Ni, Gallenkamp *et al.*^{5,6}

With an axial Cl^- ligand, the nominal ground state of the pyridinic models is more variable: with model sizes 1 and 2, an intermediate spin electronic structure is clearly favored, while at sizes 3 and 4 low spin becomes preferred. These low spin states are better characterized as pseudo-Fe(II) states resulting from an internal redox event. At model size 5, all three spin states are found within 1.5 kcal/mol of each other, high spin being the lowest. Nevertheless, the isomer shift predicted across all model sizes is ca. 0.4 mm/s and varies only within the uncertainty range. The quadrupole splitting for the low spin electronic structure is converged already at model size 3. The preferred high spin state at model size 5 has the same quadrupole splitting value as the intermediate spin states of model sizes 3, 4, 5 within the uncertainty range.

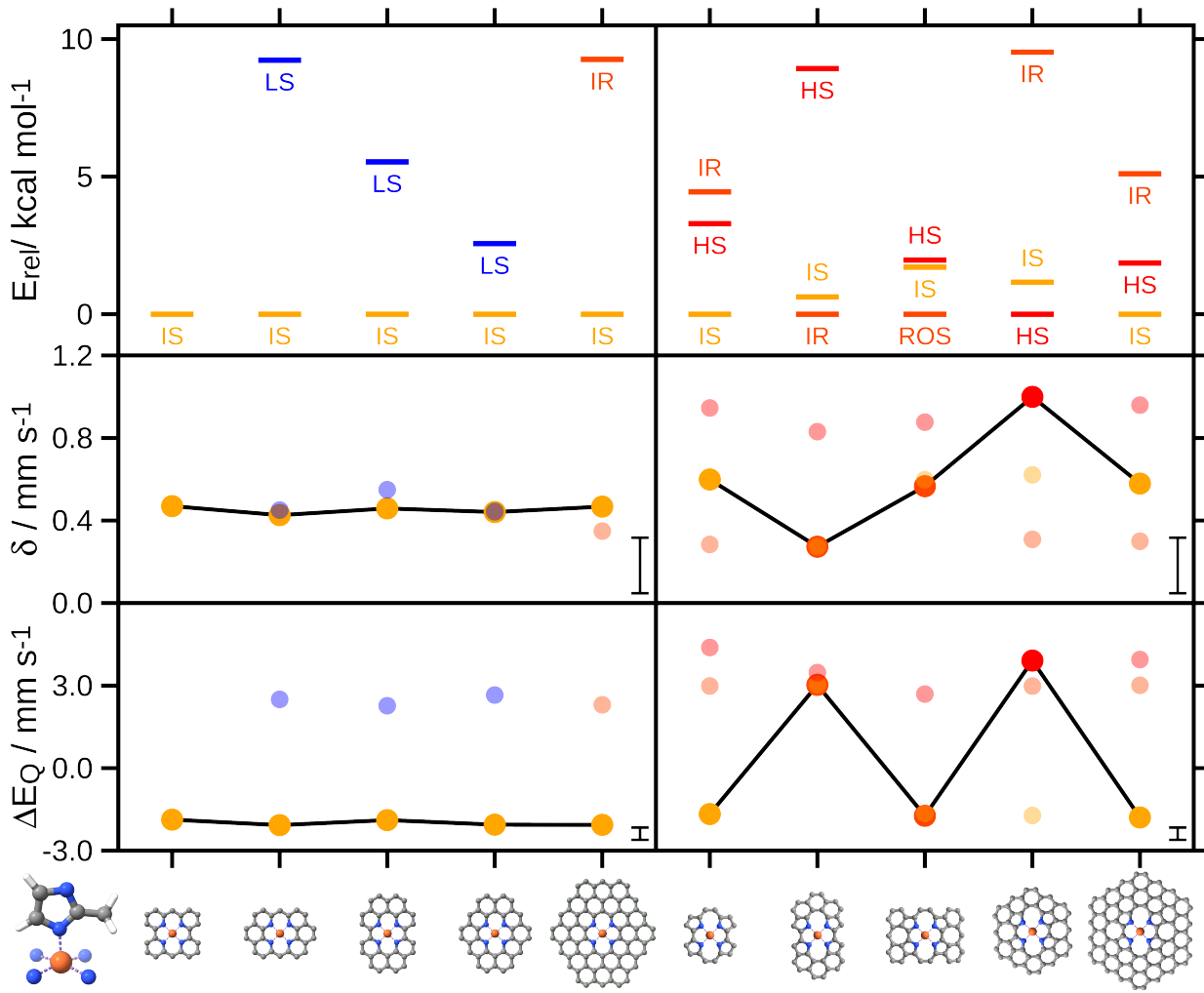


Figure 7 Evolution of spin state energetics (top) and Mössbauer parameters (middle, bottom) of fivefold coordinated neutral models A-2-MeHIm (left panels) and B-2-MeHIm (right panels). In the upper panels, all states with a relative energy $< 10 \text{ kcal mol}^{-1}$ are shown, labeled according to Figure 2. The connected data points correspond to the electronic ground state; the unconnected, transparent data points to energetically low-lying configurations. Low spin states are shown in blue, intermediate spin states in yellow, “true” high spin states (HS) in dark red and intramolecular-redox (IR) or ring-open-shell (ROS) high spin states (corresponding to HS 2 and HS 3 in the fourfold-coordinated models) in bright red. Uncertainty ranges of the respective Mössbauer parameters are shown in the lower right corners.

In B-Cl, intermediate and high spin states are accessible for nearly all model sizes, whereas low spin states are destabilized. For model size 3 and larger, the gap between the high spin and intermediate spin configurations is less than 1.5 kcal/mol. The isomer shift is found around 0.33 mm/s (except for model size 3 at 0.66 mm s^{-1}) and varies only within the uncertainty range for all models. The quadrupole splitting for the intermediate spin ground state is converged at model size 4.

Comparing the Mössbauer values predicted for both types of model with different axial ligands, it can be concluded that computational models can be used to distinguish different speciations of FeNC active sites. This mirrors previous findings in the literature, including our own.^{6,11,20,30,31,44,87,89}

Next, we investigate the role of the 2-MeHIm and Cl^- ligands on the spin state in our periodic model. For that 6×6 pyridinic and pyrrolic structures with the ligand bound to iron were fully relaxed using GGA and GGA+U. Binding an axial ligand results in lifting the iron atom from the carbon plane,

though to different degrees. In the relaxed pyrrolic structure with 2-MeHIm, the iron atom is significantly elevated by 1.33 \AA (0.80 \AA) above the carbon plane, whereas in the relaxed pyridinic structure, it remains much closer at 0.34 \AA (0.39 \AA) using GGA+U (GGA). For the Cl ligand, the iron atom is displaced by 1.27 \AA (0.86 \AA) in the pyrrolic structure and 1.0 \AA (0.33 \AA) in the pyridinic structure using GGA+U (GGA).

These different structures using different density functional theory approaches also lead to different predicted ground spin states. With the GGA approach, intermediate spin states are favoured. For the pyridinic structure with the 2-MeHIm ligand, $M_{tot} = 1.96 \mu_B$ is found, while the pyrrolic structure exhibits M_{tot} of $2.24 \mu_B$ due to significant hybridisation with the nearest nitrogen atom in the ligand. Similarly for the Cl^- ligand, a ground IS configuration with M_{tot} of $3.0 \mu_B$ is found for the pyrrolic structure, while M_{tot} of $1.05 \mu_B$ was calculated for the pyridinic structure. The GGA+U results indicate that all cases converge to a high spin state with M_{tot} of about $4.0 \mu_B$ corre-

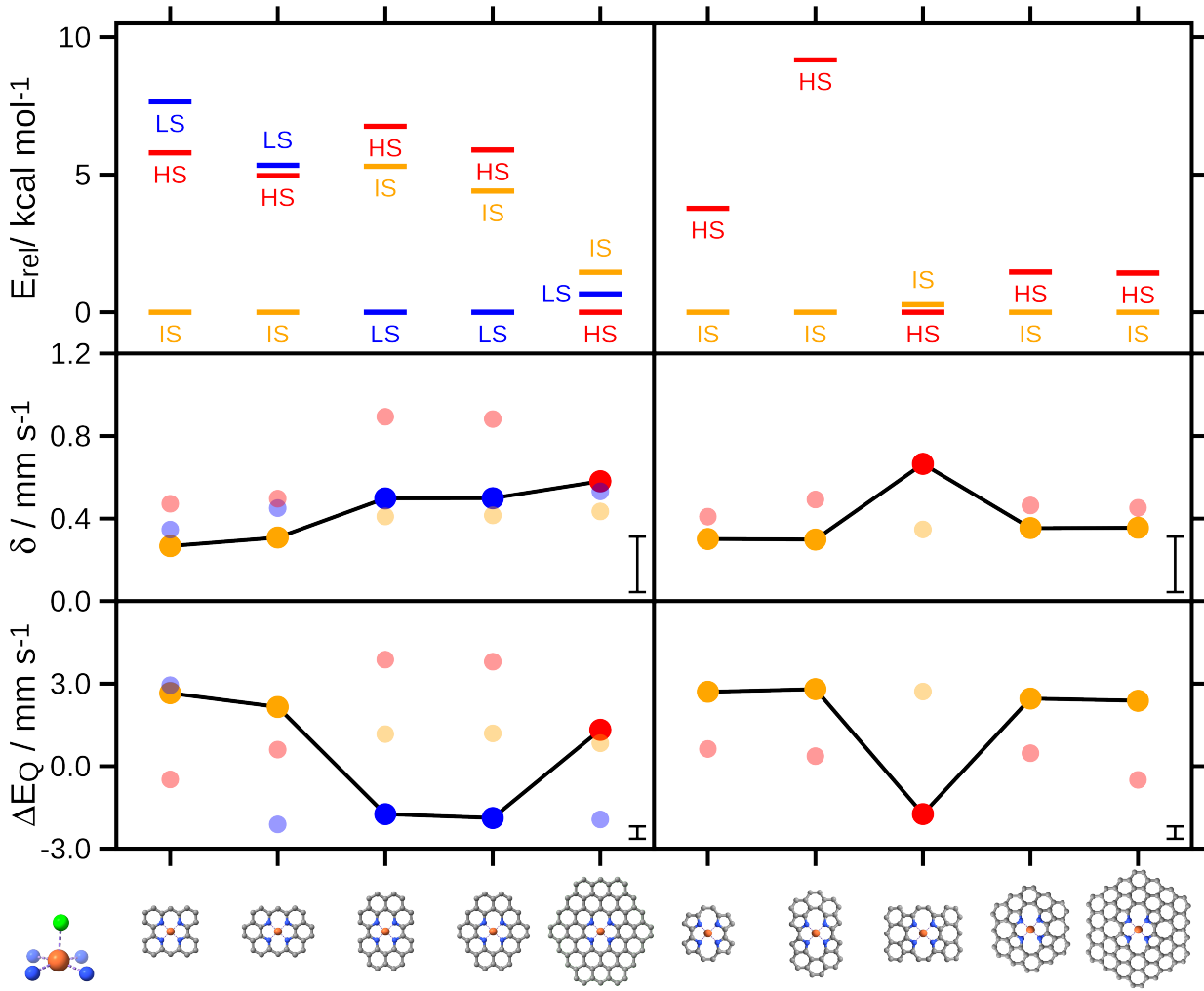


Figure 8 Evolution of spin state energetics (top) and Mössbauer parameters (middle, bottom) of fivefold coordinated neutral models A-Cl (left panels) and B-Cl (right panels). In the upper panels, all states with a relative energy < 10 kcal mol⁻¹ are shown, labeled according to Figure 2. The connected data points correspond to the electronic ground state; the unconnected, transparent data points to energetically low-lying configurations. Low spin states are shown in blue, intermediate spin states in yellow, high spin states in red. Uncertainty ranges of the respective Mössbauer parameters are shown in the lower right corners.

sponding to $2S + 1 = 5$ for the 2-MeHIm ligand. With the Cl⁻ ligand, the ground state of the pyrrolic structure is found to have $M_{tot} = 5.00 \mu_B$, while $M_{tot} = 3.12 \mu_B$ is obtained for the pyridinic structure.

These findings highlight that the periodic models with both types of axial ligands predict an HS configuration for both pyridinic and pyrrolic structures when including proper correlation effects in the calculations. Each relaxed structure shows substantial displacement of iron from the carbon layer, similar to the OOP phase of the square-planar models, which stabilizes the calculated spin configurations. In contrast, the more standard approach of using a pure GGA formalism consistently prefers an IS state associated with smaller iron displacements. This emphasizes that the structural composition of the active site model as well as the computational approach need to be developed carefully for meaningful comparisons with experimental data.

4 Conclusion

Considering that traditional structural elucidations of the active sites of single atom catalysts fall short, the community relies on computational models to better understand the properties and reactivities of these promising materials. Herein, we presented an extensive study of the spatial scope and electronic complexity of active sites in FeNC models using molecular and periodic models.

A key finding is that square-planar coordination environments cannot support an Fe(II) high spin configuration. Models of this type therefore cannot be used to explain the experimental observation of this type of Mössbauer signature. A chemically meaningful model with an Fe(II) high spin configuration requires for the iron atom to be lifted outside the plane of the equatorial carbon environment. This can be achieved in molecular tetracoordinate models by introducing defects that lead to a curved graphene environment. Differences between the spin state predictions of molecular and periodic models were traced back to structural differences, most importantly the enforced

planarity of the periodic models. For a periodic model with an out-of-plane iron in a pyrrolic environment, a high spin configuration was found, albeit at slightly higher energy than the in-plane model. A similar type of curvature can be present in carbon nanotubes, which are best described with a periodic approach. Alternatively, axial ligands can be bound at iron, which also lift it from the graphene-based plane and alter the ligand field splitting such that high spin states become energetically accessible.

Regarding the convergence of spin states and Mössbauer properties, we showed that molecular models should incorporate at least two complete rings of carbon atoms around the FeN₄ unit, while periodic models should have at least a size of 6×6. Most importantly though, we identified several types of electronic structure that are relevant for iron in FeNC-type environments. Besides the expected low spin, intermediate spin and high spin configurations in which the unpaired electrons are confined to the d-orbitals, we found energetically relevant electronic structures with unpaired electrons in the carbon environment. These may be a result of intramolecular redox events, i.e. reduction or oxidation of the graphene π-system leading to a net electron transfer from or to the iron ion, or ferromagnetic or antiferromagnetic coupling between a formal triplet configuration of the graphene π-system with the unpaired electrons in the iron d-orbitals.

In many cases, several distinct electronic structures are found within a small energy window. These highly complex electronic structures would ideally be treated with multiconfigurational approaches, which is however outside the scope of studies that aim to understand the catalytic behaviour of single-atom catalysts. In terms of assignments to the experimentally observed Mössbauer signatures, we emphasize that unpaired electrons in the graphene environment do not lead to different isomer shift or quadrupole splitting values. Nevertheless, we expect that such electronic structure details can be important for catalysis, as was recently suggested for a hydrogen evolution catalysis with molecular porphyrin complexes^{50,90}.

Overall, our findings show that the results from both molecular and periodic models are in good agreement with each other and experimental data. Besides designing a chemically meaningful structural model, future studies should ensure that a high quality of electronic structure description is used to avoid artefacts, e.g. GGA+U with a benchmarked value for U, or carefully chosen hybrid functionals. By leveraging the strengths of both molecular and periodic approaches, a comprehensive understanding of the energetics of possible spin states of iron and the corresponding Mössbauer parameters can be obtained. This information as well as other spectroscopic properties provide a direct point of comparison with experimental data on FeNC catalysts under *ex situ*, *in situ* and *operando* conditions.

Author Contributions

Conceptualisation: CG, RV, VK; Data Curation: CG, YJS, NvR, GLM; Visualization: NvR, YJS, GLM; Validation, formal analysis, writing: CG, YJS, NvR, GLM, RV, VK; Supervision: RV, VK.

Conflicts of interest

There are no conflicts to declare.

Acknowledgements

This work was funded by the Deutsche Forschungsgemeinschaft (DFG, German Research Foundation) – CRC 1487, “Iron, upgraded!” – project number 443703006. NvR further acknowledges funding by the Deutsche Bundesstiftung Umwelt (DBU) and NvR, CG and VK acknowledge computational resources provided by the Lichtenberg high performance cluster at the NHR Centers NHR4CES at TU Darmstadt.

Notes and references

- [1] P. Gupta, B. Toksha and M. Rahaman, *Chemical record* (New York, N.Y.), 2024, **24**, e202300295.
- [2] M. K. Singla, P. Nijhawan and A. S. Oberoi, *Environmental science and pollution research international*, 2021, **28**, 15607–15626.
- [3] H. Zhang, H. T. Chung, D. A. Cullen, S. Wagner, U. I. Kramm, K. L. More, P. Zelenay and G. Wu, *Energy & Environmental Science*, 2019, **12**, 2548–2558.
- [4] D. J. S. Sandbeck, N. M. Secher, M. Inaba, J. Quinson, J. E. Sørensen, J. Kibsgaard, A. Zana, F. Bizzotto, F. D. Speck, M. T. Y. Paul, A. Dworzak, C. Dosche, M. Oezaslan, I. Chorkendorff, M. Arenz and S. Cherevko, *Journal of The Electrochemical Society*, 2020, **167**, 164501.
- [5] L. Ni, C. Gallenkamp, S. Paul, M. Kübler, P. Theis, S. Chabarra, K. Hofmann, E. Bill, A. Schnegg, B. Albert, V. Krewald and U. I. Kramm, *Advanced Energy and Sustainability Research*, 2021, **2**, 2000064.
- [6] L. Ni, C. Gallenkamp, S. Wagner, E. Bill, V. Krewald and U. I. Kramm, *Journal of the American Chemical Society*, 2022, **144**, 16827–16840.
- [7] K. Kumar, L. Dubau, F. Jaouen and F. Maillard, *Chemical reviews*, 2023, **123**, 9265–9326.
- [8] J. Kibsgaard, A. Jackson and T. F. Jaramillo, *Nano Energy*, 2016, **29**, 243–248.
- [9] S. Haller, V. Gridin, K. Hofmann, R. W. Stark, B. Albert and U. I. Kramm, *Energy Technology*, 2021, **9**, 2001106.
- [10] *N4-Macrocyclic Metal Complexes*, ed. J. H. Zagal, F. Bedioui and J.-P. Dodelet, Springer New York, New York, NY, 2006.
- [11] C. Gallenkamp, U. I. Kramm, J. Proppe and V. Krewald, *International Journal Quantum Chemistry*, 2020, 26394, 1–19.
- [12] A. Zitolo, V. Goellner, V. Armel, M.-T. Sougrati, T. Mineva, L. Stievano, E. Fonda and F. Jaouen, *Nature Materials*, 2015, **14**, 937–942.
- [13] E. Proietti, F. Jaouen, M. Lefèvre, N. Larouche, J. Tian, J. Herranz and J.-P. Dodelet, *Nature Communications*, 2011, **2**, 416.
- [14] J. Li, S. Ghoshal, W. Liang, M.-T. Sougrati, F. Jaouen, B. Halevi, S. McKinney, G. McCool, C. Ma, X. Yuan, Z.-F. Ma, S. Mukerjee and Q. Jia, *Energy & Environmental Science*, 2016, **9**, 2418–2432.

- [15] A. Pedersen, A. Bagger, J. Barrio, F. Maillard, I. E. L. Stephens and M.-M. Titirici, *J. Mater. Chem. A*, 2023, **11**, 23211–23222.
- [16] N. Ohri, Y. Hua, R. Baidoun and D. Kim, *Chem Catalysis*, 2023, **3**, 100837.
- [17] L. Osmieri, R. K. Ahluwalia, X. Wang, H. T. Chung, X. Yin, A. J. Kropf, J. Park, D. A. Cullen, K. L. More, P. Zelenay, D. J. Myers and K. C. Neyerlin, *Applied Catalysis B: Environmental*, 2019, **257**, 117929.
- [18] V. A. Saveleva, M. Retegan, K. Kumar, F. Maillard and P. Glatzel, *J. Mater. Chem. A*, 2023, **11**, 18862–18871.
- [19] J. L. Kneebone, S. L. Daifuku, J. A. Kehl, G. Wu, H. T. Chung, M. Y. Hu, E. E. Alp, K. L. More, P. Zelenay, E. F. Holby and M. L. Neidig, *The Journal of Physical Chemistry C*, 2017, **121**, 16283–16290.
- [20] D. Menga, J. L. Low, Y.-S. Li, I. Arčon, B. Koyutürk, F. Wagner, F. Ruiz-Zepeda, M. Gaberšček, B. Paulus and T.-P. Fellinger, *Journal of the American Chemical Society*, 2021, **143**, 18010–18019.
- [21] D. Menga, F. E. Wagner and T.-P. Fellinger, *Materials horizons*, 2023, **10**, 5577–5583.
- [22] J. S. Bates, J. J. Martinez, M. N. Hall, A. A. Al-Omari, E. Murphy, Y. Zeng, F. Luo, M. Primsb, D. Menga, N. Bibent, M. T. Sougrati, F. E. Wagner, P. Atanassov, G. Wu, P. Strasser, T.-P. Fellinger, F. Jaouen, T. W. Root and S. S. Stahl, *Journal of the American Chemical Society*, 2023, **145**, 26222–26237.
- [23] M. T. Sougrati, V. Goellner, A. K. Schuppert, L. Stievano and F. Jaouen, *Catalysis Today*, 2016, **262**, 110–120.
- [24] P. Gütlich, *Chemie in unserer Zeit*, 1970, **4**, 133–144.
- [25] P. Gütlich, *Chemie in unserer Zeit*, 1971, **5**, 131–141.
- [26] P. Gütlich, E. Bill and A. X. Trautwein, *Mössbauer Spectroscopy and Transition Metal Chemistry: Fundamentals and Applications*, Springer Berlin Heidelberg, Berlin, Heidelberg, 2011.
- [27] E. Bill, *Practical Approaches to Biological Inorganic Chemistry (Second Edition)*, Elsevier, Second Edition edn, 2020, pp. 201–228.
- [28] N. von Rhein and V. Krewald, *Chem. Commun.*, 2025, **61**, 2512–2515.
- [29] J. L. Low, C. Roth and B. Paulus, *The Journal of Physical Chemistry C*, 2024, **128**, 5075–5083.
- [30] C. Gallenkamp, U. I. Kramm and V. Krewald, *JACS Au*, 2024, **4**, 940–950.
- [31] J. Li, M. T. Sougrati, A. Zitolo, J. M. Ablett, I. C. Oğuz, T. Mineva, I. Matanovic, P. Atanassov, Y. Huang, I. Zenyuk, A. Di Cicco, K. Kumar, L. Dubau, F. Maillard, G. Dražić and F. Jaouen, *Nature Catalysis*, 2021, **4**, 10–19.
- [32] X. Li, C.-S. Cao, S.-F. Hung, Y.-R. Lu, W. Cai, A. I. Rykov, S. Miao, S. Xi, H. Yang, Z. Hu, J. Wang, J. Zhao, E. E. Alp, W. Xu, T.-S. Chan, H. Chen, Q. Xiong, H. Xiao, Y. Huang, J. Li, T. Zhang and B. Liu, *Chem*, 2020, **6**, 3440–3454.
- [33] X. Zhang, Z. Xia, H. Li, S. Yu, S. Wang and G. Sun, *New Journal of Chemistry*, 2020, **44**, 6818–6824.
- [34] P. Nematollahi, B. Barbiellini, A. Bansil, D. Lamoen, J. Qingying, S. Mukerjee and E. C. Neyts, *ACS Catalysis*, 2022, **12**, 7541–7549.
- [35] P. Nematollahi and E. C. Neyts, *The Journal of Physical Chemistry C*, 2022, **126**, 14460–14469.
- [36] Y.-J. Song, C. Gallenkamp, G. Lleopart, V. Krewald and R. Valentí, *Physical chemistry chemical physics : PCCP*, 2024, **26**, 26370–26376.
- [37] B. Henderson, S. Donnecke, S. N. Genin, I. G. Ryabinkin and I. Paci, *The Journal of Physical Chemistry C*, 2024, **128**, 15899–15911.
- [38] S. Yu, Z. Levell, Z. Jiang, X. Zhao and Y. Liu, *Journal of the American Chemical Society*, 2023, **145**, 25352–25356.
- [39] D. Menga, J. L. Low, A. G. Buzanich, B. Paulus and T.-P. Fellinger, *Advanced Energy Materials*, 2024, 2400482.
- [40] N. Yang, L. Peng, L. Li, J. Li, Q. Liao, M. Shao and Z. Wei, *Chemical science*, 2021, **12**, 12476–12484.
- [41] I. C. Oğuz, F. Jaouen and T. Mineva, *Molecules (Basel, Switzerland)*, 2024, **29**, 479.
- [42] W. Liu, S. Ye and Le Shi, *ACS applied materials & interfaces*, 2025, **17**, 4895–4903.
- [43] T. Zheng, J. Wang, Z. Xia, G. Wang and Z. Duan, *J. Mater. Chem. A*, 2023, **11**, 19360–19373.
- [44] J. L. Low and B. Paulus, *Catalysts*, 2023, **13**, 566.
- [45] J. Xie and Z. Duan, *The Journal of Physical Chemistry C*, 2024, **128**, 20819–20826.
- [46] J. R. Sams and T. B. Tsin, *The Porphyrins*, Academic Press, 1979, pp. 425–478.
- [47] D. Dolphin, J. R. Sams, T. B. Tsin and K. L. Wong, *Journal of the American Chemical Society*, 1976, **98**, 6970–6975.
- [48] Y. Ohgo, S. Neya, T. Ikeue, M. Takahashi, M. Takeda, N. Funasaki and M. Nakamura, *Inorganic Chemistry*, 2002, **41**, 4627–4629.
- [49] C. Hu, J. An, B. C. Noll, C. E. Schulz and W. R. Scheidt, *Inorganic chemistry*, 2006, **45**, 4177–4185.
- [50] N. Heppe, C. Gallenkamp, S. Paul, N. Segura-Salas, N. von Rhein, B. Kaiser, W. Jaegermann, A. Jafari, I. Sergueev, V. Krewald and U. I. Kramm, *Chemistry (Weinheim an der Bergstrasse, Germany)*, 2023, **29**, e202202465.
- [51] A. R. Groenhof, M. Swart, A. W. Ehlers and K. Lamermotsma, *The Journal of Physical Chemistry A*, 2005, **109**, 3411–3417.

- [52] M. Radoń, *Journal of chemical theory and computation*, 2014, **10**, 2306–2321.
- [53] M. Radoń, *Computational Chemistry*, Elsevier, Amsterdam, 2019, vol. 73, pp. 221–264.
- [54] G. Li Manni, D. Kats, D. P. Tew and A. Alavi, *Journal of chemical theory and computation*, 2019, **15**, 1492–1497.
- [55] M. Swart, *Journal of chemical theory and computation*, 2008, **4**, 2057–2066.
- [56] M. Güell, J. M. Luis, M. Solà and M. Swart, *The Journal of Physical Chemistry A*, 2008, **112**, 6384–6391.
- [57] R. Breglia, D. Perilli and C. Di Valentin, *Materials Today Chemistry*, 2023, **33**, 101728.
- [58] M. Pápai and G. Vankó, *Journal of Chemical Theory and Computation*, 2013, **9**, 5004–5020.
- [59] P. Hohenberg and W. Kohn, *Physical Review*, 1964, **136**, B864–B871.
- [60] W. Kohn and L. J. Sham, *Physical Review*, 1965, **140**, A1133–A1138.
- [61] F. Neese, *WIREs Computational Molecular Science*, 2012, **2**, 73–78.
- [62] F. Neese, F. Wennmohs, D. Aravena, M. Atanasov, Auer, Alexander A., Becker, Ute, G. Bistoni, D. Bykov and et al., *ORCA - An ab initio, DFT and semiempirical SCF-MO package - Version 5.0.3: Manual*.
- [63] A. V. Marenich, C. J. Cramer and D. G. Truhlar, *Journal of Physical Chemistry B*, 2009, **113**, 6378–6396.
- [64] F. Neese, F. Wennmohs, A. Hansen and U. Becker, *Chemical Physics*, 2009, **356**, 98–109.
- [65] F. Weigend, *Physical Chemistry Chemical Physics*, 2006, **8**, 1057–1065.
- [66] J. Tao, J. P. Perdew, V. N. Staroverov and G. E. Scuseria, *Physical Review Letters*, 2003, **91**, 146401.
- [67] F. Weigend and R. Ahlrichs, *Physical Chemistry Chemical Physics*, 2005, **7**, 3297–3305.
- [68] S. Grimme, J. Antony, S. Ehrlich and H. Krieg, *Journal of Chemical Physics*, 2010, **132**, 154104, 1–19.
- [69] S. Grimme, S. Ehrlich and L. Goerigk, *Journal of Computational Chemistry*, 2011, **32**, 1456–1465.
- [70] J. P. Perdew, K. Burke and M. Ernzerhof, *Phys. Rev. Lett.*, 1996, **77**, 3865–3868.
- [71] N. C. Handy and A. J. Cohen, *Molecular Physics*, 2001, **99**, 403–412.
- [72] C. T. Lee, W. T. Yang and R. G. Parr, *Physical Review B*, 1988, **37**, 785–789.
- [73] F. Neese, *Inorganica Chimica Acta*, 2002, **337**, 181–192.
- [74] A. D. Becke, *Journal of Chemical Physics*, 1993, **98**, 5648–5652.
- [75] E. F. Pettersen, T. D. Goddard, C. C. Huang, E. C. Meng, G. S. Couch, T. I. Croll, J. H. Morris and T. E. Ferrin, *Protein science : a publication of the Protein Society*, 2021, **30**, 70–82.
- [76] P. E. Blöchl, *Phys. Rev. B*, 1994, **50**, 17953–17979.
- [77] G. Kresse and J. Furthmüller, *Phys. Rev. B*, 1996, **54**, 11169–11186.
- [78] S. L. Dudarev, G. A. Botton, S. Y. Savrasov, C. J. Humphreys and A. P. Sutton, *Phys. Rev. B*, 1998, **57**, 1505–1509.
- [79] M. R. A. Blomberg, P. E. M. Siegbahn and M. Svensson, *The Journal of Chemical Physics*, 1996, **104**, 9546–9554.
- [80] V. Blum, R. Gehrke, F. Hanke, P. Havu, V. Havu, X. Ren, K. Reuter and M. Scheffler, *Computer Physics Communications*, 2009, **180**, 2175–2196.
- [81] S. R. Jensen, S. Saha, J. A. Flores-Livas, W. Huhn, V. Blum, S. Goedecker and L. Frediani, *The Journal of Physical Chemistry Letters*, 2017, **8**, 1449–1457.
- [82] P. Borlido, T. Aull, A. W. Huran, F. Tran, M. A. L. Marques and S. Botti, *Journal of Chemical Theory and Computation*, 2019, **15**, 5069–5079.
- [83] S. Kokott, F. Merz, Y. Yao, C. Carbogno, M. Rossi, V. Havu, M. Rampp, M. Scheffler and V. Blum, *The Journal of Chemical Physics*, 2024, **161**, 024112.
- [84] P. Chaudhuri, C. N. Verani, E. Bill, E. Bothe, T. Weyhermüller and K. Wieghardt, *Journal of the American Chemical Society*, 2001, **123**, 2213–2223.
- [85] P. J. Chirik and K. Wieghardt, *Science (New York, N.Y.)*, 2010, **327**, 794–795.
- [86] W. Kaim and B. Schwederski, *Coordination Chemistry Reviews*, 2010, **254**, 1580–1588.
- [87] N. von Rhein, J. L. Low, C. Gallenkamp, B. Paulus and V. Krewald, *ChemRxIV*, 2025, 10.26434/chemrxiv-2025-9hstm-v2.
- [88] V. I. Anisimov, J. Zaanen and O. K. Andersen, *Phys. Rev. B*, 1991, **44**, 943–954.
- [89] J. Barrio, A. Pedersen, S. C. Sarma, A. Bagger, M. Gong, S. Favero, C.-X. Zhao, R. Garcia-Serres, A. Y. Li, Q. Zhang, F. Jaouen, F. Maillard, A. Kucernak, I. E. L. Stephens and M.-M. Titirici, *Advanced materials (Deerfield Beach, Fla.)*, 2023, **35**, e2211022.
- [90] N. Heppe, C. Gallenkamp, R. Z. Snitkoff-Sol, S. D. Paul, N. Segura-Salas, H. Haak, D. C. Moritz, B. Kaiser, W. Jaegermann, V. Potapkin, A. Jafari, V. Schünemann, O. Leupold, L. Elbaz, V. Krewald and U. I. Kramm, *Journal of the American Chemical Society*, 2024, **146**, 12496–12510.